Static self energy and effective mass of the homogeneous electron gas from Quantum Monte Carlo calculations

Markus Holzmann, Francesco Calcavecchia, David M. Ceperley, Valerio Olevano

Static self energy and effective mass of the homogeneous electron gas from Quantum Monte Carlo calculations

Markus Holzmann,[1] Francesco Calcavecchia,[1] David M. Ceperley,[2] and Valerio Olevano[3]

[1] *Univ. Grenoble Alpes, CNRS, LPMMC, 38000 Grenoble, France*
[2] *University of Illinois Urbana-Champaign,Urbana, Illinois 61801, USA*
[3] *CNRS, Institut Néel, 38042 Grenoble, France*

(Dated: May 3, 2023)

We discuss the methodology of quantum Monte Carlo calculations of the effective mass based on the static self energy, $\Sigma(k,0)$. We then use variational Monte Carlo calculations of $\Sigma(k,0)$ of the homogeneous electron gas at various densities to obtain results very close to perturbative G_0W_0 calculations for values of the density parameter $1 \le r_s \le 10$. The obtained values for the effective mass are close to diagrammatic Monte Carlo results and disagree with previous quantum Monte Carlo calculations based on a heuristic mapping of excitation energies to those of an ideal gas.

PACS numbers:

Landau's Fermi liquid theory [1] has provided a paradigmatic frame for the phenomenological description of equilibrium and transport properties of degenerate fermions in terms of a very few characteristic parameters. Silin [2] has provided the path to generalize for long-range forces, in order to extend it to normal metals in condensed matter [3, 4]. Although the formal structure of the underlying microscopic theory has been known for a long time [5–7], most explicit calculations of the Fermi liquid parameters rely on approximative, perturbative schemes [8, 9]. As diagrammatic perturbation theory is not expected to converge for typical electronic densities, basic Fermi liquid parameters of the 3D homogeneous electron gas (jellium), such as the effective mass m^* and the renormalization factor Z, are sensitive to the underlying approximation [10].

Recently, variational diagrammatic Monte Carlo calculations (VDiagMC) [11, 12] for 3D jellium have been performed to include and control higher order terms of the perturbation series. Those calculations found an overall reasonable agreement for Z with previous quantum Monte Carlo calculations (QMC) [13]. However, VDiagMC results on m^* have been strongly questioned by QMC calculations of Ref. [14] yielding substantially different values.

In this paper, we revisit the methodology of zero temperature QMC calculations of the effective mass, in order to resolve the discrepancy between QMC and perturbative/VDiagMC results, show how such calculations can be done and provide new results for 3D Jellium. In principle, the effective mass can also be calculated from the temperature dependence of thermodynamic quantities [15, 16], e.g. from finite-temperature path-integral results [17–19]; finite temperature methods will not be discussed here. In contrast to systems with short range interaction [20], size corrections are expected to play an important role for charged systems [21] as explained in detail below.

Landau energy functional. Landau [1] phenomenologically characterized the low energy excitation of a Fermi liquid by assuming a one-to-one correspondence of states of the ideal Fermi gas and those of the interacting system, such that elementary excitations of the interacting systems are still described in terms of ideal gas occupation numbers before adiabatically switching on the interaction. Changes of the total energy, δE, can then be considered as a functional of changes in the quasi-particle occupation number $\delta n_{p\sigma}$ of the momentum p and spin quantum number σ

$$\delta E = \sum_{p\sigma} (\varepsilon_p + \mu)\delta n_{p\sigma} + \frac{1}{2V} \sum_{p\sigma,p'\sigma'} f(p\sigma,p'\sigma')\delta n_{p\sigma}\delta n_{p'\sigma'} \tag{1}$$

Here, μ is the chemical potential, $\varepsilon_p = (p - p_F)p_F/m^*$ is the quasiparticle energy which determines the effective mass for momenta in the vicinity of the Fermi momentum, p_F, and $f(p\sigma,p'\sigma')$ is the quasi-particle interaction, independent of volume, V, to leading order. Here, and in the following, we assume a homogeneous system with isotropic Fermi surface.

The success of Landau's Fermi liquid theory started with its application to strongly interacting quantum liquids [22]. Postulating an entropy functional in terms of quasi-particle occupations, non-trivial predictions could be made using only a few parameters, notably the effective mass as a coefficient of the quasi-particle energy ε_p.

Fermi liquid behavior results from the assumption of certain analytical properties of fundamental correlation functions [7], notably the existence of a Fermi surface [6] defined by the sharp discontinuity Z of the momentum distribution at zero temperature, and the effective mass m^* obtained from the dispersion of the quasi-particle peak of the spectral function.

Both quantities, Z and m^*, can thus be operationally defined from the single particle Greens function, conve-

niently expressed in Fourier space,

$$G(k,z) = G^+(k,z) + G^-(k,z) \quad (2)$$

$$G^\pm(k,z) = \sum_n \frac{|\langle E_n^{N\pm1}|a_k^\dagger|E_0^N\rangle|^2}{z-(\pm(E_n^{N\pm1}-E_0^N)-\mu)} \quad (3)$$

where $|E_n^N\rangle$ denotes the n^{th} eigenstate with energy E_n^N of the N-particle system. The self energy Σ defined as

$$G^{-1}(k,z) = z+\mu-k^2/2m-\Sigma(k,z) \quad (4)$$

captures all effects of interactions where m is the bare mass. The Fermi surface is then determined from $G^{-1}(k_F,0)=0$, or $\mu = k_F^2/2m + \Sigma(k_F,0)$. Its analytic structure close to the singularity determines Fermi liquid behavior. Under quite general assumptions the self-energy of the infinite system allows an expansion [7]

$$\Sigma(k,z)-\Sigma(k_F,0) = (k-k_F)\partial_k\Sigma(k_F,0) + z\partial_z\Sigma(k_F,0) \quad (5)$$

up to corrections of order k^2 and $z^2\log z$. The singularity dominating the Green's function close to the Fermi surface is then

$$G(k,z) \sim \frac{Z}{z-(k-k_F)k_F/m^*} \quad (6)$$

with

$$Z^{-1} = 1-\partial_z\Sigma(k_F,0) \quad (7)$$

$$\frac{m}{m^*} = Z\left(1+\frac{m}{k_F}\partial_k\Sigma(k_F,0)\right) \quad (8)$$

giving rise to a well defined quasi-particle behavior of strength Z and energy $(k-k_F)k_F/m^*$. Since $G(k,0)$ changes sign at $k=k_F$, the singularity of the Green's function close to the Fermi surface is entirely contained in either $G^+(k,z)$ or $G^-(k,z)$. The real-time spectral function is obtained by approaching the real axis using $z=i\omega+\eta_k$ where $\eta_k=+0$ (-0) for $k>k_F$ $(k<k_F)$.

Landau's energy functional may then be identified with the quasi-particle energies of the single particle propagator [4, 6], providing a microscopic expression for the quasi-particle occupation number [4, 7]. As knowledge of the quasi-particle energy is explicitly required and its definition involves off-diagonal matrix elements in the energy eigenstate representation, this definition is purely formal and has not been of much practical use. However, it provides a strong indication that Landau's quasi-particle occupation number may not be expressible as a simple static observable whose value can be determined from a single energy eigenstate. Only in the limit $k\to k_F$, does the quasi-particle energy approximate an exact energy eigenstate up to corrections of the order of the inverse lifetime [7], provided the thermodynamic limit is taken first.

Both, Z and m^*, can be obtained from static observables at zero temperature. The value of the renormalization constant Z can be read off from the jump in the momentum distribution [13], whereas $\Sigma(k,0)$ can be obtained from the static response to an external perturbation $\xi(a_k+a_k^\dagger)$ as we will show below. Together they can be used to calculate m^* very near to the Fermi surface.

Landau's Fermi liquid theory successfully describes thermal equilibrium or hydrodynamic transport observables [22], i.e. bulk properties. The form of Landau's energy functional, Eq. (1), assures that its energy changes with respect to variation of the quasi-particle occupations are to first order additive, with corrections from a small, $\sim 1/V$, pairwise interaction. Although these energy variations can be mapped to variations of the unperturbed ideal gas propagator within adiabatic perturbation theory [7], they cannot, in general, be mapped to the exact excited energy eigenstates of the interacting system.

The microscopic theory maps them to the single particle quasi-particle spectrum, characterized by the emerging pole in the exact interacting propagator, Eq. (6), when approaching the real axis, $z=i\omega+\eta_k$ with $\eta_k\to\pm0$. However, for any finite system, the exact Green's function, Eq. (2) is a highly irregular function on the real axis; a smooth function can only be expected a finite distance from the real axis, $|\eta_k| \gtrapprox k_F 2\pi/(mL)$. Instead, the effective mass formula, Eq. (8), involves only static quantities with $z=0$ and are well defined on the real axis, even before the thermodynamic limit is performed. Their calculations may still suffer from important finite-size effects [21], but numerical extrapolations will eventually converge to the infinite system size values.

Considering the generalized Hamiltonian $\tilde{H} = \sum_N (H_N-\mu N)$, an external perturbation $\xi(a_k+a_k^\dagger)$ couples the ground state of the N particle systems to excitations containing $N\pm1$ particles. From time-independent perturbation theory, restricting to states $|E^+\rangle$ within the subspace of N and $N+1$ particles, the perturbed ground state up to linear order in ξ can be written as

$$|E_k^+(\xi)\rangle = |E_0^N\rangle - \xi\sum_n \frac{|E_n^{N+1}\rangle\langle E_n^{N+1}|a_k^\dagger|E_0^N\rangle}{E_n^{N+1}-E_0^N-\mu} \quad (9)$$

yielding the energy to second order in ξ:

$$E_k^+(\xi) = E_0^N+\mu-\xi^2\sum_n \frac{|\langle E_n^{N+1}|a_k^\dagger|E_0^N\rangle|^2}{E_n^{N+1}-E_0^N-\mu}. \quad (10)$$

Similarly E_k^- is the ground state of the perturbed Hamiltonian restricted to the N and $N-1$ subspaces. The Green's functions are determined by comparing with the Lehmann representation, Eq. (2),

$$G^\pm(k,0) = \lim_{\xi\to0}\left[\pm(E_k^\pm(\xi)-E_0^N)-\mu\right]/\xi^2. \quad (11)$$

Upper bounds to the ground state energies $E_k^\pm$ can be obtained with a variational ansatz for $|E_k^\pm\rangle$ and minimizing the expectation value of the perturbed Hamiltonian with respected to variational parameters. Although

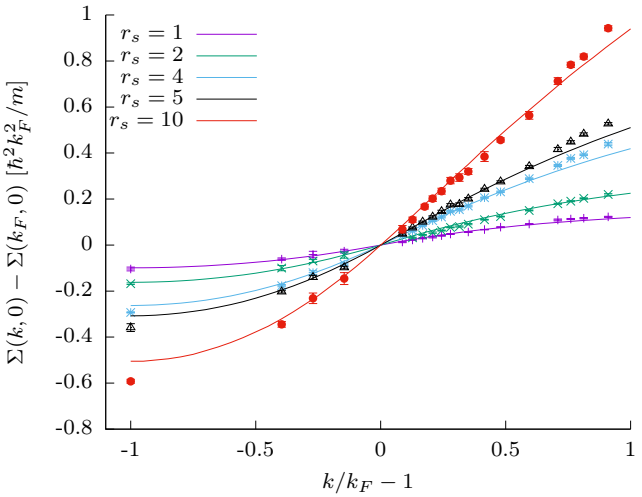

FIG. 1: Static self-energy for various densities (r_s) using backflow (BF) trial wave functions and GC-TABC simulations for $N = 38$ electrons. They include size corrections. The color lines are from G_0W_0 calculations.

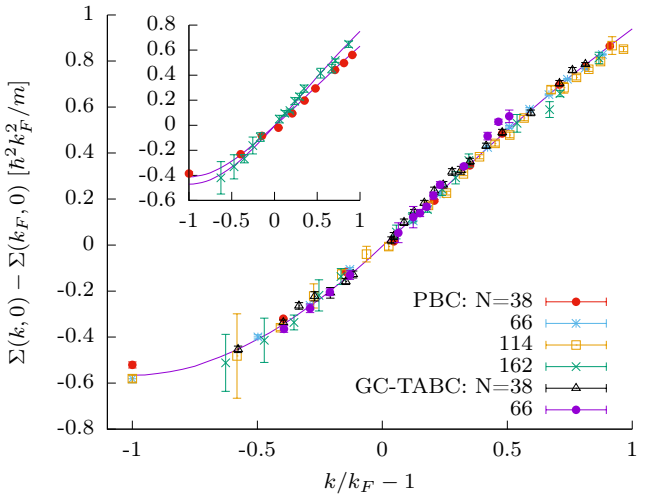

FIG. 2: Static self-energy for $r_s = 10$ using SJ-VMC trial wave functions for simulations with periodic boundary conditions (PBC) and GC-TABC for various sizes ranging from $N = 38$ to $N = 162$, size corrected according to Eq. (17), the line is a fit to the data. The inset shows the uncorrected values for $N = 38$ and $N = 162$ (PBC), the lines indicate the size corrections of the fit based on Eq. 17).

technically a little bit more involved, calculations of the static Green's function is thereby reduced to a static response function, analogous to calculations of the density response [23] previously employed using ground state Monte Carlo methods.

Quantum Monte Carlo calculations. Let us now turn to the calculation of the static single-particle Green's function via quantum Monte Carlo methods, focusing on $G^+(k,0)$. For that, we minimize the energy $E_T^+(\xi)$ of the generalized Hamiltonian $\widetilde{H}$ using a trial wave function, $|\Psi_T(\xi)\rangle$, in the Fock space of N and $N+1$ particle wave functions providing an upper bound for $E_k^+(\xi)$.

Assuming that ξ is sufficiently small, the trial wave function can be expanded as

$$|\Psi_T(\xi)\rangle = |\Psi_0^N\rangle + \xi \sum_{i=1}^{M} \alpha_i |\Psi_i^{N+1}\rangle \qquad (12)$$

with M the number of states in the basis. It couples the ground state wave function $|\Psi_0^N\rangle$ of the N particle system (or our best variational ground state wave function) with different wave functions $|\Psi_i^{N+1}\rangle$ of the $N+1$ particle states of total momentum corresponding to k. The variational parameters are the set $\{\alpha_i\}$. A minimal choice consists in choosing $M = 2$, with $|\Psi_1^{N+1}\rangle$ as a candidate for a pure excited state wave function, minimizing separately the excited state energy E_k^{N+1} in the $N+1$ section of momentum k, and $|\Psi_2^{N+1}\rangle \sim a_k^\dagger |\Psi_0^N\rangle$; this should maximize the overlap matrix elements of the perturbation with the ground state.

Minimizing with respect to α_1, α_2 in the limit of $\xi \to 0$, we obtain a variational approximation for the Green's function in the particle excitation sector

$$G_\mu^+(k,0) = -\frac{\zeta_1^2 \varepsilon_{22} - 2\zeta_1\zeta_2\varepsilon_{12} + \zeta_2^2\varepsilon_{11}}{\varepsilon_{11}\varepsilon_{22} - \varepsilon_{12}^2} \qquad (13)$$

$$\text{with} \quad \varepsilon_{ij} = \langle \Psi_i^{N+1} | H_{N+1} - E_0^N - \mu | \Psi_j^{N+1} \rangle \qquad (14)$$

$$\zeta_i = \langle \Psi_i^{N+1} | a_k^\dagger | \Psi_0^N \rangle \qquad (15)$$

where we have assumed normalized wave functions, e.g. $\langle \Psi_i^{N\pm1} | \Psi_i^{\pm} \rangle = 1$, with overall phases such that all matrix elements are real.

An analogous calculation in the hole sector yields $G_\mu^-(k,0)$ from a variational calculation based on superposition of the lowest energy state for a hole excitation and $a_k|\Psi_0^N\rangle$. Thus, the static Green's function $G_\mu(k,0) = G_\mu^+(k,0) + G_\mu^-(k,0)$ is determined.

So far, the chemical potential, μ, entering as a parameter in $G_\mu^\pm$, has not been specified yet. Since single particle excitation are gapless in the Fermi liquid, the chemical potential can be fixed by the implicit equation $\lim_{k\to k_F} G_\mu^{-1}(k,0) = 0$.

Finite size effects. Our Quantum Monte Carlo calculations are done for finite number of electrons N confined in a periodic cube of side L and volume $V = L^3$. Calculations must be extrapolated to the thermodynamic limit. Shell effects in the single particle energy spectrum and the Coulombic interaction represent the main source of finite size effects [24].

Shell effects can be addressed by twisted boundary conditions [25] corresponding to a shifted grid calculation in momentum space. Using grand-canonical twist averaging (GC-TABC) [26] we obtain a sharp Fermi surface. We

spherically average $G^{\pm}_{\mu}(k,0)$ for any k using 32 equally weighted points that exactly integrates all polynomials on the sphere up to the eighth order [27, 28].

Although GC-TABC allows us to obtain $G^{\pm}_{\mu}(k,0)$ for arbitrary k, size effects due to intrinsic two-body effects remain. In charged systems, these are dominated by the long-range Coulomb interaction [29]. In particular, z_k and n_k are expected to suffer from important size effects [13] of order $1/L$. Instead of addressing them directly which necessitates a thorough investigation as a function of L and k, we will determine the exact leading order form of the corrections from a diagrammatic analysis based on Fermi liquid theory [7]. Following Ref. [21], within the RPA approximation, $\delta\Sigma(k,0) = \Sigma_{\infty}(k,0) - \Sigma_N(k,0)$ is given by

$$\delta\Sigma(k,0) \simeq -\int_{-\pi/L}^{\pi/L} \frac{d^3q}{(2\pi)^3} \int_{-\infty}^{\infty} \frac{d\nu}{(2\pi)} \frac{v_q}{\epsilon(q,i\nu)} \frac{1}{i\nu + \mu - \varepsilon^0_{k+q}} \tag{16}$$

where $v_q = 4\pi e^2/q^2$ is the Coulomb interaction, $\varepsilon^0_k = \hbar^2k^2/2m$, and the integral is restricted to a cube with $|q_\alpha| < \pi/L$ for any spatial component ($\alpha = x, y, z$). Due to this restriction, we can use the expression $\epsilon(q,\omega) \simeq 1 - \omega_p^2/\omega$ for the dielectric function, where ω_p is the plasma frequency. Since, the dominant contribution to the integral stems from the finite values of $\omega = i\nu$, substituting this limiting form for the dielectric function captures the exact behavior in the limit of small q. The resulting integration then gives

$$\delta\Sigma(k,0) = C\frac{\varepsilon^0_k - \mu}{\omega_p + |\varepsilon^0_k - \mu|} \tag{17}$$

with $C \simeq 1.22\, e^2/L$. One can show that Eq. (17) is indeed exact not only within RPA, if $\varepsilon^0_k - \mu$ is replaced by the exact single particle energies $(k-k_F)k_F/m^*$. This occurs since irreducible vertex corrections approach $1/Z$ in the limit of vanishing momentum transfer at fixed frequency [7] and exactly cancel against the quasiparticle weight of the exact propagator replacing the non-interacting propagator in the RPA expression.

Results and discussion. We have performed VMC calculations for the 3D homogeneous electron gas based on analytical Slater-Jastrow (SJ) and Slater-Jastrow backflow (BF) wave functions [30] as used in a previous study on the renormalization factor [13]. Its density, n, is parametrized by $r_s \equiv a/a_B$, where a_B is the Bohr radius and $a = (4\pi n/3)^{-1/3}$ is the mean electron distance. Details of the VMC procedure are given in the Supplementary Material.

In Figure 2 we illustrate the importance of size effects at $r_s = 10$, comparing canonical simulations with periodic boundary conditions (PBC) from system sizes, $N = 38$ to 114 using SJ wave functions. Although, the bare curves seem to indicate only small variations with size, the size corrected curves based on the analytical formula above show that the bare curves for such small systems are still very far from reaching the thermodynamic limit. Due to the slow decay $\sim L$ of the corrections, we have not attempted any numerical extrapolation of the curves,. Extrapolation is more difficult for smaller values of r_s since variations are masked by the larger stochastic error.

r_s	method	Z	$mk_F^{-1}\partial_k\Sigma$	m^*/m
1	BF-VMC	0.86(1) [13]	$0.17^{0.18}_{0.15}(1)$	$1.00^{1.01}_{0.99}(1)$
	SJ-VMC	0.894(9) [13]	$0.17^{0.18}_{0.15}(1)$	$0.96^{0.97}_{0.95}(1)$
	G_0W_0 (RPA)	0.859 [31]	0.200	0.970 [10]
	VDiagMC [12]	0.8725(2)	0.200(1)	0.955(1)
2	BF-VMC	0.78(1)	$0.309^{0.361}_{0.280}(6)$	$0.98^{1.00}_{0.94}(1)$
	SJ-VMC	0.82(1)	$0.30^{0.31}_{0.28}(2)$	$0.94^{0.95}_{0.93}(2)$
	G_0W_0 (RPA)	0.768 [31]	0.313	0.992 [10]
	VDiagMC [12]	0.7984(2)	0.328(4)	0.943(3)
4	BF-VMC	0.65(1)	$0.538^{0.549}_{0.530}(7)$	$1.00^{1.01}_{0.99}(2)$
	SJ-VMC	0.69(1)	$0.55_{0.45}(2)$	$0.94^{1.00}(2)$
	G_0W_0 (RPA)	0.646 [31]	0.490	1.039 [10]
	VDiagMC [12]	0.6571(2)	0.528(5)	0.996(3)
5	BF-VMC	0.59(1)	$0.56^{0.65}(1)$	$1.09_{1.03}(3)$
	SJ-VMC	0.61(1)	$0.610^{0.624}_{0.596}(9)$	$1.02^{1.03}_{1.01}(2)$
	G_0W_0 (RPA)	0.602 [31]	0.569	1.059 [10]
10	BF-VMC	0.41(1)	$0.90^{0.98}_{0.88}(2)$	$1.28^{1.30}_{1.23}(3)$
	SJ-VMC	0.45(1)	$0.97^{1.03}_{0.91}(3)$	$1.13^{1.16}_{1.09}(3)$
	G_0W_0 (RPA)	0.45 [31]	0.98	1.13

TABLE I: Our QMC results with backflow (BF) and Slater-Jastrow (SJ) trial functions as compared to those of G_0W_0 (RPA) and variational diagrammatic Monte Carlo (VDiagMC) [12, 32, 33]. Upper and low indices indicate systematic errors assuming different fitting functions/ranges to determine $\partial_k\Sigma(k_F,0)$.

In Figure (1) we compare our size corrected results from BF-VMC calculations using grand-canonical twist averaging to perturbative G_0W_0 results. Even though $r_s = 10$ is thought to be far outside the range of validity of a perturbative approach our QMC results indicate only small modifications in the whole range $r_s \leq 10$; differences are hardly visible on the figures.

In contrast to Z, perturbative calculations of $\partial_k\Sigma(k_F,0)$ seem to be much less sensitive to the underlying approximation scheme, e.g. self-consistency and vertex corrections [34, 35]. We do not believe that the quantitative agreement of the static self energy between QMC and G_0W_0 is a result of fortuitous error cancellations.

In order to deduce the effective mass, we have fitted our QMC results for $\Sigma(k,0)$ around k_F to obtain $\partial_k\Sigma(k_F,0)$. In table I we summarize our results based on size corrected GC-TABC calculations for $N = 66$ SJ and $N = 54$ BF wave functions. We see that the decrease of Z competes with the increase of $\partial_k\Sigma(k_F,0)$,

resulting in values of m^*/m very close to one. However, since $mk_F^{-1}\partial_k\Sigma(k_F,0)$ remains smaller than one even at $r_s = 10$, the lowering of Z with increasing r_s eventually dominates the effective mass and m^* clearly increases for $r_s \gtrsim 4$.

Similarly to Z, the change from the SJ trial function to more accurate BF trial functions reduces $\partial_k\Sigma(k_F,0)$ by a small amount, slightly larger than our statistical resolution. This provides a rough estimate of the bias due to the trial wave function. Since our approach is variational, we expect that the our results provide upper bounds to $\partial_k\Sigma$. In addition, more correlated wave functions tend to lower the values of Z [13, 36], so that our results for m^* are likely lower bounds. Future studies based on iterative backflow and machine learning wave functions [36–38] can be used to further reduce the wave function bias.

Our results are in rather good agreement with perturbative G_0W_0 calculations [10, 31] and more recent variational digrammatic Monte Carlo calculations including higher order diagrams [12, 32]. They are at variance with previous QMC calculations [14] of m^* which are based on a heuristic mapping of excitation energies to the ideal gas and not on the properties of the single particle Green's function. As we have reviewed above, the use of Landau's energy functional to determine Fermi liquid parameters from the excitation spectrum of finite systems is highly problematic. The comparison with those results is further detailed in the Supplementary Material.

The quantitative agreement between two methodologically and numerically different methods, real space QMC and VDiagMC, is highly encouraging. Comparisons with high precision measurements, as already done in solid sodium [39] and lithium [40, 41] for the renormalization factor, Z, can now be extended to the band width and effective mass.

The authors acknowledge support from the Fondation Nanosciences de Grenoble. DMC is supported by the U.S. Dept. of Energy, CMS program DE-SC0020177. M.H. thanks Saverio Moroni for many valuable discussions. Computations were done using the GRICAD infrastructure which is supported by Grenoble research communities, and HPC resources from GENCI-IDRIS A0140914158.

Supplementary Material

In this Supplementary Material we provide details of the VMC calculations, how the self-energy is extracted, and how errors are estimated. Then we present data for different sizes of the simulation cell in table S.2. Finally we compute an effective band mass of excitation energies and compare with a recent calculation.

Variational Monte Carlo Simulations

We have performed variational quantum Monte Carlo simulations using both Γ point and grand-canonical twist-averaged boundary conditions (GC-TABC) conditions for systems containing between $N = 38$ and $N = 162$ electrons. In these calculations we used Slater-Jastrow (SJ) and Slater-Jastrow-Backflow (BF) trial wave functions with analytical expressions for the Jastrow and backflow potentials as detailed in Ref. [30] for the 3D jellium, and used in a previous calculation for momentum distribution [13] and for the renormalization factor Z entering the effective mass formula.

Wave function structure

A SJ/BF wave function for the ground state is

$$\Psi_0^N = D_k^N e^{-U_N} \tag{S.18}$$

with

$$D^N = \det_{qn} \varphi_q(r_n) \tag{S.19}$$

$$\varphi_q(r) = e^{iq\cdot r} \tag{S.20}$$

where q contains N wave vectors of lowest $|q|$ (here and in the following we do not explicitly consider the spin-structure of our paramagnetic system where the determinant can be further reduced to the product of two determinants, one for each spin), and U_N denotes the symmetric pair correlation factor

$$U_N = \sum_{i<j} u(r_i - r_j) \tag{S.21}$$

In the case of SJ wave functions, the arguments of the orbitals $\varphi_q(\cdot)$ are the bare electron coordinates, whereas in backflow wave functions they are shifted by a many-body correlation factor [30].

Our perturbed wave functions, Eq. (12), is then built from the SJ (BF) ground state wave function of the N particle ground state, Ψ_0^N, and from $M = 2$ non-orthogonal states, $\Psi_1^{N\pm1}$ and $\Psi_2^{N\pm1}$. To describe a perturbation of momentum k, $\Psi_{1/2}^{N\pm1}$ describe wave functions where essentially a plane wave orbital of wave vector k is added/removed from the N particle ground state. The amount of correlation changes between $\Psi_1^{N\pm1}$ and $\Psi_2^{N\pm1}$. In the following, we describe both wave functions in detail.

Let us first discuss $\Psi_1^{N\pm1}$ which is chosen in order to represent a good trial wave function for an $N\pm1$ particle energy state with momentum $\pm k$ compared to the ground state. For $\Psi_1^{N\pm1}$, we used the simplest extension of the ground state state wave function to a correlated excited

state which approximately describes an exact eigenstate of momentum $\pm k$ in the $N \pm 1$ particle sector

$$\Psi_1^{N\pm1} = D_k^{N\pm1} e^{-U_{N\pm1}} \tag{S.22}$$

In the case of particle excitations (Ψ_1^{N+1}), the orbitals of the Slater determinant D^{N+1} now contain also k in addition to all wave vectors occupied in the ground state, whereas for hole excitations (Ψ_1^{N-1}), the orbital of wave vector k is removed. Further, $U_{N\pm1}$ denotes the symmetric pair correlation potential

$$U_{N\pm1} = \sum_{i<j} u(r_i - r_j) \tag{S.23}$$

which is built from the same Jastrow potential $u(\cdot)$ used in the ground state, and the summation is over all $N(N\pm1)/2$ pairs of particles.

In contrast to $\Psi_1^{N\pm1}$, where we have used a straightforward candidate for minimizing the total energy,

$$E_{11}^{N\pm1} \equiv \frac{\langle \Psi_1^{N\pm1} | H_{N\pm1} | \Psi_1^{N\pm1} \rangle}{\langle \Psi_1^{N\pm1} | \Psi_1^{N\pm1} \rangle} \tag{S.24}$$

$\Psi_2^{N\pm1}$ is chosen to maximize the overlap with the perturbation acting on the ground state, $a_k^\dagger |\Psi_0^N\rangle$. The natural candidate is then to directly use a state $|\Psi_2^{N+1}\rangle \propto a_k^\dagger |\Psi_0^N\rangle$ in the case of particle excitations, and $|\Psi_2^{N-1}\rangle \propto a_k |\Psi_0^N\rangle$ for holes.

In the coordinate representation, the unnormalized hole state Ψ_2^{N-1} can be written as

$$\Psi_2^{N-1}(\mathbf{R}_{N-1}) = \int d\mathbf{r}_n e^{-ik\cdot r_N} \Psi_0^N(\mathbf{R}_N) \tag{S.25}$$

with $\mathbf{R}_N = (\mathbf{r}_1, \ldots, \mathbf{r}_N)$.

In practice, we perform a VMC calculation of weight $|\Psi_1^{N-1}(\mathbf{R}_{N-1})|^2$, and matrix elements/ expectation values containing $\Psi_0^N(\mathbf{R}_N)$ and $\Psi_2^{N-1}(\mathbf{R}_{N-1})$ can be accessed via introducing additional integrals over $\mathbf{r}_N$ and reweighting.

In the particle excitation sector, Ψ_2^{N+1}, for SJ wave functions, we can explicitly write down $|\Psi_2^{N+1}\rangle \propto a_k^\dagger |\Psi_0^N\rangle$ in the coordinate representation

$$\Psi_2^{N+1}(\mathbf{R}_{N+1}) = \sum_n \frac{\delta D_k^{N+1}}{\delta \varphi_k(\mathbf{r}_n)} \varphi_k(\mathbf{r}_n) e^{-U_N^n(\mathbf{R}_{N+1})} \tag{S.26}$$

where

$$U_N^n(\mathbf{R}_{N+1}) \equiv \sum_{i<j, i,j\neq n} u(r_i - r_j) = U_{N+1}(\mathbf{R}_{N+1}) - \widetilde{u}(r_n) \tag{S.27}$$

$$\widetilde{u}(r) = \sum_{i=1}^{N+1} u(r_i - r) - u(0) \tag{S.28}$$

and we can write

$$\Psi_2^{N+1}(\mathbf{R}_{N+1}) = \sum_n \frac{\delta D_k^{N+1}}{\delta \varphi_k(\mathbf{r}_n)} \varphi_k(\mathbf{r}_n) e^{\widetilde{u}(r_n)} e^{-U_{N+1}(\mathbf{R}_{N+1})} \tag{S.29}$$

Denoting $\widetilde{\varphi}_k(r) = \varphi_k(r) \exp[\widetilde{u}(r)]$ for the orbital k, we can write the wave function in form of a determinant times a symmetric correlation function

$$\Psi_2^{N+1}(\mathbf{R}_{N+1}) = \det_{qn} \widetilde{\varphi}_q(r_n) e^{-U_{N+1}(\mathbf{R}_{N+1})} \tag{S.30}$$

with $\widetilde{\varphi}_q(r) = \varphi_q(r)$ for $q \neq k$. Derivatives of the determinant needed for the local energy can be calculated similarly as backflow [42, 43].

In the case of BF, we have used Eq. (S.30) where the bare coordinates are replaced by the backflow coordinates constructed exactly as in the $N+1$ particle case. Although this wave function is not exactly proportional to $a_k^\dagger |\Psi_0^N\rangle$, we don't expect any significant differences, e.g. we have checked that $|\langle \Psi_2^{N+1} | a_k^\dagger | \Psi_0^N \rangle|^2$ coincides with $\langle \Psi_0 | a a_k^\dagger | \Psi_0^N \rangle = 1 - n_k$ within our stochastic error.

GC-TABC

In the GC-TABC procedure [24, 26, 44] the volume of the simulation box is fixed by $V = N/n$ where n is the electronic density. Each simulation is characterized by a twist vector; the phase that the trial function picks up as an electron exits the supercell on one side and re-enters the other side. For a given twist vector, the Slater determinant of our wave function consists of all plane wave states of wave vector $\mathbf{k}$ such that $|\mathbf{k}| \leq k_F$. The number of electrons then depends on the twist vector, N_θ, but the number of electrons averaged over all twists equals N. Expectation values of observables and matrix elements are calculated independently for each twist angle and then averaged over twists. In all our simulations N has been chosen to be one that has a closed shell ground state at the Γ point.

Notice that all our trial wave functions have the properties that by space inversion they equal their complex conjugate, hence the overlap integrals and matrix elements are real.

For our study of the static self-energy, $\Sigma(k, 0)$, for any given k and twist angle, the observables and matrix elements ε_{ij}, z_k, and n_k, given by Eq.(14),(15), and (16) as well as the ground state energy E_0 have been calculated from a variational Monte Carlo run with weight $|\Psi_1^{N+1}|^2$ using reweighting. (The equivalent procedure in the hole sector with $|\Psi_1^{N-1}|^2$.) Within GC-TABC, the expectation values are twist averaged before inserting them into the expression of the Greens function, Eq.(13). Note that Eq.(13) depends parametrically on the chemical potential μ, but the Monte Carlo expectation values depend trivially on μ. For canonical VMC calculations at the Γ point, values of k are on a discrete grid given by the number of electrons N. Continuous values of k are only reached in the limit of $N \to \infty$.

For GC-TABC, any k vector can be reached by imposing the corresponding twist angle. Spherical averaging

over all k vectors of given magnitude then corresponds to averaging twist over all twist angles yielding the same modulus of k. In our GC-TABC calculations, we have used 32 equally weighted points that exactly integrates all polynomials on the sphere up to order eight [27, 28] for any given value of k. Typically we have performed simulations for around ~ 10 different k values around k_F in our runs for each N. In the GC-TABC runs we have chosen similar values of k as the canonical runs where the k values are fixed by N. We also chose some intermediate ones to interpolate better between them. In our GC-TABC runs, we have avoided k vectors too close to k_F, in particular the region $|k - k_F| \lesssim \pi/L$ where no excitation would be possible in a canonical simulation, since inside that region twist averaging can produce artifacts in the self-energy. In any case, since the perturbed energies approaches $E_0 \pm \mu$ for $k \to k_F$, the finite precision of our Monte Carlo evaluations additionally limit calculations approaching too closely the Fermi surface.

Estimation of Self-energy

Given the value of the chemical potential, μ, the Greens functions $G^{\pm}_{\mu}$ can be expressed in terms of QMC observables, e.g. Eq.(13-16) in the main text, (and thereby $\Sigma_\mu(k,0)$) by subtracting the single particle energies. Its value at the Fermi surface, $\Sigma_\mu(k_F,0)$, as well as the slope of the self-energy have been obtained by linear and quadratic fits around k_F. The value of μ is then varied so that $\Sigma_\mu(k_F,0) = \mu$. In table S.2, μ_N and $\partial_k\Sigma_N$ indicate the values obtained before size extrapolation. This procedure has been performed for the bare values at given system size, N, and, equally, using the extrapolated self-energy $\Sigma^{\infty}_{\mu}(k,0) = \Sigma_\mu(k,0) + \delta\Sigma(k,0)$, using Eq. (18). In the table (which one), μ_∞ and $\partial_k\Sigma_\infty$ correspond to the chemical potential and the slope obtained using extrapolated self-energies extrapolated.

Estimation of Errors

Since all matrix elements needed for the Greens function/ self-energy are calculated within the same QMC simulations, the errors are not independent. Therefore, we have estimated the final uncertainty of our self-energy, by determining its spread over several independent calculations and different twist angles in GC-TABC.

The systematic errors for all quantities given in the tables are estimated by looking at how the χ^2 value varies with respect to the fitted value. Fits of GC-TABC curves usually yield values of χ^2 close to one per degree of freedom. The χ^2 value of the fits for canonical simulations at the Γ point are typically larger, in particular for the $N = 38$ and $N = 66$ systems, because of the irregular filling of the shells of states, and the fewer k values close to k_F.

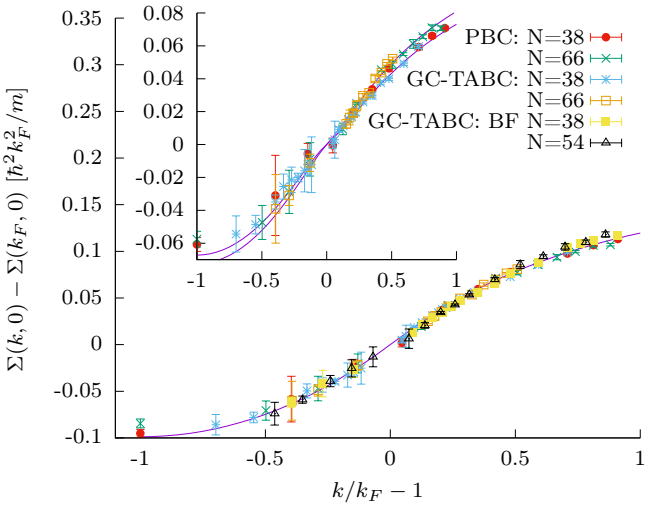

FIG. S.3: Static self-energy for $r_s = 1$ using SJ-VMC trial wave functions for simulations with periodic boundary conditions (PBC) and GC-TABC for $N = 38$ and $N = 66$ together with those from BF-VMC trial wave functions with GC-TABC $N = 38$ and $N = 54$. All curves in the main plot are size corrected according to Eq. (17) of main text, the line is the G_0W_0 self energy. The inset shows the uncorrected values (only SJ for clarity), the lines show the size corrections based on Eq. (17) of the main text on the G_0W_0 curve.

Finite Size Data

In the table of the main text, we have reported SJ and BF values from size extrapolated GC-TABC using systems with $N = 66$, and $N = 54$, respectively. Due to the systematic uncertainty of results with different sizes, we did not attempt further numerical extrapolation. Table S.2 reports the data without size-corrections.

In Fig. S.3 we further illustrate the changes due to size corrections for the self-energy at $r_s = 1$.

Comparison with Reference [14]

In Ref. [14] an apparent effective mass was determined assuming a mapping between energy eigenstates and occupations of the orbitals used in SJ and BF wave functions in the spirit of Landau's energy functional. As we have outlined in the main text, relating quasi-particle energies to exact energy eigenstates of a finite system, though highly intuitive, is problematic and without firm theoretical justification. Differences our our values of m^* compared to those given in Ref. [14] are therefore mainly due to the different methodology used here, and not to differences in the VMC wave functions, nor to the use of

r_s	Ψ	BC	N	μ_N	μ_∞	$mk_F^{-1}\partial_k\Sigma_N$	$mk_F^{-1}\partial_k\Sigma_\infty$
1	SJ	Γ	38	$0.6224^{0.632}_{0.618}(8)$	$0.628^{0.637}_{0.626}(3)$	$0.095^{0.114}_{0.068}(3)$	$0.18^{0.20}_{0.16}(1)$
			66	$0.628^{0.632}_{0.623}(1)$	$0.629^{0.641}_{0.627}(4)$	$0.108^{0.112}_{0.091}(4)$	$0.18^{0.20}_{0.16}(2)$
		GC-TABC	38	$0.632^{0.634}_{0.621}(1)$	$0.634^{0.639}_{0.623}(1)$	$0.089^{0.117}_{0.079}(4)$	$0.182^{0.22}_{0.14}(6)$
			66	$0.634^{0.635}_{0.629}(3)$	$0.635^{0.640}_{0.632}(2)$	$0.09^{0.11}_{0.08}(2)$	$0.17^{0.18}_{0.16}(1)$
	BF	GC-TABC	38	$0.628^{0.629}_{0.623}(1)$	$0.633^{0.637}_{0.628}(2)$	$0.086^{0.097}_{0.077}(8)$	$0.17^{0.18}_{0.15}(1)$
			54	$0.628^{0.629}_{0.619}(1)$	$0.634^{0.637}_{0.622}(4)$	$0.097^{0.112}_{0.078}(4)$	$0.167^{0.179}_{0.157}(4)$
2	SJ	Γ	38	$0.2082^{0.2090}_{0.2070}(5)$	$0.2110_{0.2088}(5)$	$0.190^{0.207}_{0.185}(4)$	$0.334^{0.370}(4)$
			66	$0.235^{0.241}_{0.222}(2)$	$0.250^{0.251}_{0.230}(2)$	$0.173^{0.218}_{0.150}(6)$	$0.260^{0.33}(6)$
		GC-TABC	38	$0.230^{0.232}_{0.222}(1)$	$0.234^{0.240}_{0.221}(1)$	$0.168^{0.165}_{0.183}(5)$	$0.310^{0.336}_{0.300}(5)$
			66	$0.233^{0.234}_{0.226}(2)$	$0.237^{0.243}_{0.238}(4)$	$0.186^{0.190}_{0.167}(5)$	$0.30^{0.31}_{0.28}(2)$
	BF	GC-TABC	38	$0.226^{0.233}_{0.217}(2)$	$0.233^{0.235}_{0.226}(2)$	$0.15^{0.18}_{0.13}(1)$	$0.28^{0.29}(1)$
			54	$0.212^{0.215}_{0.206}(1)$	$0.219_{0.209}(2)$	$0.201^{0.227}_{0.161}(4)$	$0.309^{0.361}_{0.280}(6)$
4	SJ	Γ	38	$-0.660^{-0.656}(1)$	$-0.655^{-0.654}_{-0.656}(1)$	$0.312_{0.279}(3)$	$0.511^{0.555}_{0.457}(3)$
			66	$-0.638^{-0.631}_{-0.650}(7)$	$-0.636^{-0.625}_{-0.646}(7)$	$0.32^{0.37}_{0.28}(3)$	$0.50^{0.56}_{0.47}(3)$
		GC-TABC	38	$-0.633^{-0.629}_{-0.644}(2)$	$-0.628^{-0.622}_{-0.644}(1)$	$0.32^{0.30}_{0.34}(1)$	$0.53^{0.57}_{0.51}(1)$
			66	$-0.633^{-0.628}_{-0.646}(3)$	$-0.632^{-0.623}_{-0.650}(4)$	$0.35^{0.37}_{0.31}(1)$	$0.55_{0.45}(2)$
	BF	GC-TABC	38	$-0.653^{-0.652}_{-0.661}(2)$	$-0.649^{-0.645}_{-0.663}(2)$	$0.285^{0.301}_{0.278}(8)$	$0.51^{0.52}_{0.48}(1)$
			54	$-0.668^{-0.661}_{-0.672}(3)$	$-0.666^{-0.656}_{-0.671}(2)$	$0.34^{0.36}_{0.31}(1)$	$0.538^{0.549}_{0.491}(7)$
5	SJ	Γ	38	$-1.1137^{-1.1110}_{-1.1172}(8)$	$-1.1090^{-1.1067}_{-1.1134}(8)$	$0.357^{0.370}_{0.309}(2)$	$0.592^{0.637}_{0.530}(4)$
			66	$-1.105^{-1.100}(2)$	$-1.098^{-1.092}(2)$	$0.40_{0.38}(1)$	$0.60_{0.57}(1)$
			114	$-1.114^{-1.113}_{-1.117}(5)$	$-1.113^{-1.108}_{-1.115}(5)$	$0.43^{0.48}_{0.39}(3)$	$0.62^{0.66}_{0.58}(3)$
		GC-TABC	38	$-1.089^{-1.085}_{-1.102}(3)$	$-1.083^{-1.080}_{-1.102}(3)$	$0.38^{0.41}_{0.36}(2)$	$0.62^{0.67}_{0.61}(2)$
			66	$-1.085^{-1.082}_{-1.092}(3)$	$-1.079^{-1.078}_{-1.097}(4)$	$0.415^{0.424}_{0.390}(9)$	$0.610^{0.624}_{0.596}(9)$
			114	$-1.088^{-1.091}_{-1.072}(4)$	$-1.080^{-1.047}_{-1.088}(4)$	$0.48_{0.43}(2)$	$0.64^{0.65}_{0.56}(2)$
	BF	GC-TABC	38	$-1.114^{-1.111}_{-1.127}(2)$	$-1.105^{-1.104}_{-1.127}(2)$	$0.35^{0.36}_{0.33}(1)$	$0.573^{0.613}_{0.570}(5)$
			54	$-1.118^{-1.114}_{-1.137}(3)$	$-1.112_{-1.121}(2)$	$0.35^{0.44}(1)$	$0.56^{0.65}(1)$
10	SJ	Γ	38	$-3.510_{-3.532}(1)$	$-3.535^{-3.527}_{-3.539}(2)$	$0.604_{0.544}(2)$	$0.809^{0.891}(7)$
			66	$-3.541^{-3.540}_{-3.555}(2)$	$-3.535^{-3.527}_{-3.550}(2)$	$0.61^{0.70}(1)$	$0.91^{0.98}_{0.87}(1)$
			114	$-3.552^{-3.543}_{-3.572}(5)$	$-3.540^{-3.535}_{-3.560}(5)$	$0.66^{0.69}_{0.56}(2)$	$0.88^{0.92}_{0.81}(2)$
			162	$-3.563^{-3.533}_{-3.575}(10)$	$-3.554^{-3.533}_{-3.571}(10)$	$0.70^{0.75}_{0.62}(5)$	$0.91^{0.95}_{0.85}(5)$
		GC-TABC	38	$-3.514^{-3.507}_{-3.524}(5)$	$-3.509^{-3.504}_{-3.538}(5)$	$0.71^{0.74}_{0.65}(3)$	$1.08^{1.16}_{0.89}(3)$
			66	$-3.502^{-3.491}_{-3.535}(6)$	$-3.494^{-3.491}_{-3.522}(6)$	$0.68^{0.73}_{0.65}(2)$	$0.97^{1.03}_{0.91}(3)$
	BF	GC-TABC	38	$-3.536^{-3.534}_{-3.555}(5)$	$-3.526^{0.518}_{-3.553}(7)$	$0.58^{0.61}_{0.53}(2)$	$0.93^{0.96}_{0.86}(2)$
			54	$-3.567^{-3.563}_{-3.580}(5)$	$-3.558^{-3.553}_{-3.576}(5)$	$0.62^{0.68}_{0.57}(2)$	$0.90^{0.98}_{0.88}(2)$

TABLE S.2: Summary of various QMC calculations using Slater-Jastrow (SJ) and Slater-Jastrow backflow (BF) wave functions (Ψ) for simulations using periodic (Γ) and grand-canonical twist averaged (GC-TABC) boundary conditions (BC). Here, μ_N is the chemical potential in units of $\hbar^2k_F^2/2m$, $mk_F^{-1}\partial_k\Sigma_N$ the dimensionless slope of the self-energy at k_F, both for calculations of finite volume $\sim N$; μ_∞ and $\partial\Sigma_\infty$ denote the corresponding values obtained adding the leading finite size corrections due to the Coulomb singularity. The statistical uncertainty of the fit in the least significant digit is indicated in parentheses, whereas upper and lower indices indicate systematic shifts due to fitting range and order of the polynomial fit. Results were obtained from fitting with a linear function in a region $|k-k_F|/k_F \geq 0.2$, systematic errors by fitting with up to a quadratic function

DMC in Ref. [14] as we will shown in the following.

In our calculation of the static self energy, $\Psi_1^{N\pm1}$ was chosen to provide a reasonable approximation for an excited energy eigenstate of the $N\pm1$ particle system with momentum $\pm k$. We can therefore directly compare the energy expectation value, and in particular the "band" dispersion

$$\begin{aligned} E(k) &= \theta(|k|-k_F)\left[E_{11}^{N+1}(k)-E_0^N\right] \\ &\quad +\theta(k_F-|k|)\left[E_0^N-E_{11}^{N-1}(k)\right] \end{aligned} \tag{S.31}$$

with those given in Ref. [14].

Fitting this energy dispersion by a Padé or polynomial fit, the effective mass of Ref. [14] was determined by the

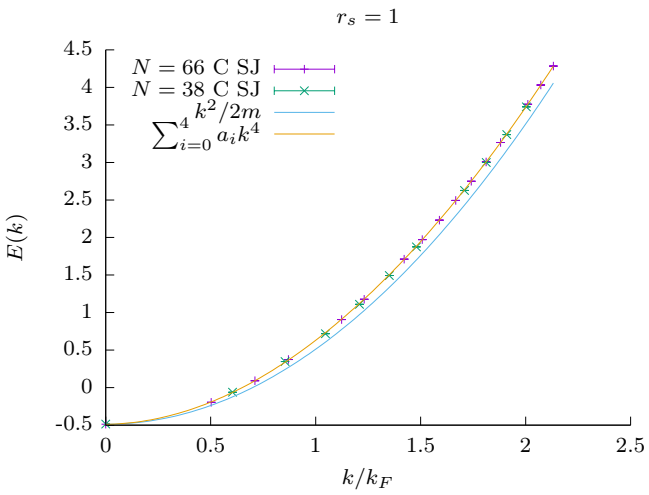

FIG. S.4: Dispersion of the energy expectation values $E(k)$ based on $\Psi_1^{N\pm1}$ for SJ wave functions for $r_s = 1$ using $N = 38$ and $N = 66$ electrons compared to the bare $k^2/2m$ behavior of non-interacting electrons. The line through our data points is based on a 4th order polynomial fit to the $N = 66$ system. From the fit at k_F we obtain $(k-k_F)k_F/m_{eff}$ with $m_{eff}/m \simeq 0.93$ close to the Fermi surface which is close to 0.915(1) given in Ref. [14] extrapolated to infinite systems sizes.

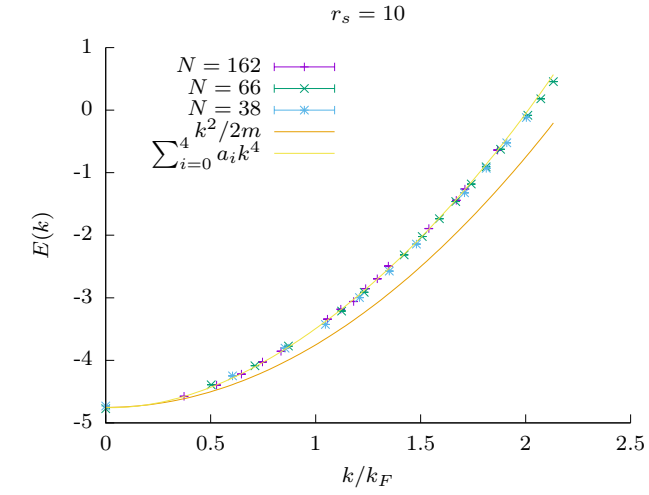

FIG. S.5: Dispersion of the energy expectation values $E(k)$ based on $\Psi_1^{N\pm1}$ for SJ wave functions for $r_s = 10$ using $N = 38$, $N = 66$, and $N = 162$ electrons compared to the bare $k^2/2m$ behavior of non-interacting electrons. The line through our data points is based on a 4th order polynomial fit to the $N = 162$ system. From the fit at k_F we obtain $(k - k_F)k_F/m_{eff}$ with $m_{eff}/m \simeq 0.83$ close to the Fermi surface. The difference to 0.75(1) given in Ref. [14] for the infinite system is compatible with the $1/N$ finite size effects shown there.

slope at the Fermi surface

$$E(k) = (|k| - k_F)k_F/m_{\rm eff}, \quad k \to k_F \tag{S.32}$$

where we denote $m_{\rm eff}$ the thus obtained "effective mass" to avoid confusion with m^* characterizing quasi-particle excitation energies.

In Figs. S.4 and S.5, we show the SJ band dispersion for $r_s = 1$ and $r_s = 10$. In agreement with the results of Ref. [14], the dispersion of the band is steeper than the one of non-interacting electrons. Using a fourth order polynomial fit for $E(k)$ of our largest systems, we get $m_{\rm eff}/m \simeq 0.93$ for $r_s = 1$, 0.90 for $r_s = 2$, 0.88 for $r_s = 4$, 0.86 for $r_s = 5$, and 0.83 for $r_s = 10$. Those values are consistent and in quantitative agreement with those of Ref. [14] at comparable sizes. Optimization of excited state wave functions as done in Ref.[14] as well as stochastic improvement via DMC make only a small change in $m_{\rm eff}$, as already noticed in Ref.[14]. Therefore the qualitative and quantitative difference of our values of m^* in table I compared to $m_{\rm eff}$ calculations [14] are due to the different methodology. The interpretation of $m_{\rm eff}$ as effective mass of quasi-particles invoking Landau's energy functional is problematic.

[1] L. D. Landau, Sov. Phys. JETP **30**, 1058 (1956).
[2] V. P. Silin, Sov. Phys. JETP **33**, 495 (1957).
[3] P. Noziéres and J. P. Luttinger, Phys. Rev. **127**, 1423 (1962).
[4] J. M. Luttinger and P. Noziéres, Phys. Rev. **127**, 1431 (1962).
[5] L. D. Landau, Sov. Phys. JETP **35**, 97 (1958).
[6] J. M. Luttinger, Phys. Rev. **119**, 1153 (1960).
[7] P. Nozières, *Theory of interacting Fermi systems*, W.A. Benjamin, Inc., New York, (1964).
[8] G. F. Giuliani and G. Vignale, Quantum Theory of the Electron Liquid (Cambridge University Press, Cambridge, 2005).
[9] R. M. Martin, L. Reining, and D. M. Ceperley, Interacting Electrons, Cambridge University Press, Cambridge (2016).
[10] G. E. Simion and G. F. Giuliani, Phys. Rev. B **77**, 035131 (2008).
[11] K. Chen and K. Haule, Nat. Commun. **10**, 3725 (2019).
[12] K. Haule and K. Chen, Scientific Reports **12**, 2294 (2022).
[13] M. Holzmann, B. Bernu, C. Pierleoni, J. McMinis, D. M. Ceperley, V. Olevano, and L. Delle Site, Phys. Rev. Lett. **107**, 110402 (2011).
[14] S. Azadi, N. D. Drummond, and W. M. C. Foulkes, Phys. Rev. Lett. **127**, 086401 (2021).
[15] F. G. Eich, M. Holzmann, and G. Vignale, Phys. Rev. B **96**, 035132 (2017).
[16] H. Xie, L. Zhang, and L. Wang, arxiv:2201.03156 (2022).
[17] E. W. Brown, B. K. Clark, J. L. DuBois, and D. M. Ceperley, Phys. Rev. Lett. **110**, 146405 (2013).
[18] E. W. Brown, J. L. DuBois, M. Holzmann, and D. M. Ceperley, Phys. Rev. B **88**, 081102(R) (2013); idem **88**,

199901(E) (2013).
[19] T. Dornheim, S. Groth, and M. Bonitz, Physics Reports **744**, 1 (2018).
[20] E. Vitali, H. Shi, M. Qin, and S. Zhang, Phys. Rev. B **94**, 085140 (2016).
[21] M. Holzmann, B. Bernu, and D. M. Ceperley, J. Phys.: Conf. Ser. **321**, 012020 (2011); arXiv:1105.2964.
[22] G. Baym and C. J. Pethick, Landau Fermi-Liquid Theory: Concepts and Applications, Wiley (2008).
[23] S. Moroni, D. M. Ceperley, and G. Senatore, Phys. Rev. Lett. **69**, 1837 (1992).
[24] M. Holzmann, R. C. Clay, M. A. Morales, N. M. Tubman, D. M. Ceperley, and C. Pierleoni, Phys. Rev. B **94**, 035126 (2016).
[25] C. Lin, F.-H. Zong, and D. M. Ceperley, Phys. Rev. E **64**, 016702 (2001).
[26] M. Holzmann, B. Bernu, V. Olevano, R. M. Martin, and D. M. Ceperley, Phys. Rev. B **79**, 041308(R) (2009).
[27] R. Womersley, Efficient Spherical Designs with Good Geometric Properties
[28] R. S. Womersley in *Contemporary Computational Mathematics - A Celebration of the 80th Birthday of Ian Sloan*, J. Dick, F. Kuo, H. Woniakowski, (eds), Spring, Cham (2018).
[29] S. Chiesa, D. M. Ceperley, R. M. Martin, and M. Holzmann, Phys. Rev. Lett. **97**, 076404 (2006).
[30] M. Holzmann, D. M. Ceperley, C. Pierleoni and K. Esler, Phys. Rev. E **68**, 046707 (2003).
[31] L. Hedin, Phys. Rev. **139**, A796 (1965).
[32] Results given in [12] are obtained at finite electronic temperature $T = T_F/25$ where T_F is the Fermi temperature and may be modified by zero temperature extrapolation.
[33] VDiagMC and G_0W_0 values for $\partial_k\Sigma_\infty$ are obtained using those given for Z and m^*/m, assuming that the respective error is statistically independent.
[34] K. Van Houcke, I. S. Tupitsyn, A. S. Mishchenko, and N. V. Prokof'ev, Phys. Rev. B **95**, 195131 (2017).
[35] A. L. Kutepov and G. Kotliar, Phys. Rev. B **96**, 035108 (2017).
[36] M. Wilson, S. Moroni, M. Holzmann, N. Gao, F. Wudarski, T. Vegge, and A. Bhowmik, arXiv:2202.04622 (2022).
[37] M. Holzmann and S. Moroni, Phys. Rev. Lett. **124**, 206404 (2020).
[38] G. Cassella, H. Sutterud, S. Azadi, N. D. Drummond, D. Pfau, J. S. Spencer, and W. M. C. Foulkes, Phys. Rev. Lett. **130**, 036401 (2023).
[39] S. Huotari, J. A. Soininen, T. Pylkkänen, K. Hämäläinen, A. Issolah, A. Titov, J. McMinis, J. Kim, K. Esler, D. M. Ceperley, M. Holzmann, and V. Olevano, Phys. Rev. Lett. **105**, 086403 (2010).
[40] N. Hiraoka, Y. Yang, T. Hagiya, A. Niozu, K. Matsuda, S. Huotari, M. Holzmann, and D. M. Ceperley, Phys. Rev. B **101**, 165124 (2020).
[41] Y. Yang, N. Hiraoka, K. Matsuda, M. Holzmann, and D.M. Ceperley, Phys. Rev. B **101**, 165125 (2020).
[42] Y. Kwon, D. M. Ceperley and R. M. Martin, Phys. Rev. **B 48**, 12037 (1993).
[43] M. Taddei, M. Ruggeri, S. Moroni and M. Holzmann, Phys. Rev. B **91**, 115106 (2015).
[44] Y. Yang, V. Gorelov, C. Pierleoni, D. M. Ceperley, and M. Holzmann, Phys. Rev. B **101**, 085115 (2020).